Journal of Materials Chemistry C

ROYAL SOCIETY OF CHEMISTRY

PAPER

View Article Online
View Journal | View Issue

Cite this: J. Mater. Chem. C, 2025, 13, 2347

Selective gas phase pulsed etching of oxides with $NbCl_5$

Juha Ojala, * Marko Vehkamäki, Mykhailo Chundak, Anton Vihervaara, Kenichiro Mizohata and Mikko Ritala *

Received 15th August 2024,
Accepted 28th November 2024

DOI: 10.1039/d4tc03488k

rsc.li/materials-c

Ta_2O_5 films were etched with $NbCl_5$ using a chemical vapor etching method known as gas-phase pulsed etching (GPPE) where the etchant is delivered in short pulses with inert gas purging in between the pulses. Arrhenius type dependence of etch per cycle (EPC) on temperature was found at 275–375 °C and the activation energy of the etching reaction is estimated at 120 kJ mol^{-1}. Length of the etchant pulse had a linear effect on EPC and increasing the purge length also increased EPC. Roughnesses of the partially etched films increased from 0.2 to 1.4 nm, as measured by atomic force microscopy. No residual Nb or Cl was detected in the films by energy-dispersive X-ray spectroscopy, but a small amount of Cl residue was seen with *in vacuo* X-ray photoelectron spectroscopy. Etching of TiO_2 and ZrO_2 was also observed but HfO_2 was not etched by $NbCl_5$ at 300–400 °C. Selectivity with respect of SiO_2, Al_2O_3, and TiN was also proven at the same temperature range. EPC up to 2.8, 1.1, and 4.0 Å were observed for Ta_2O_5, ZrO_2, and TiO_2, respectively.

1. Introduction

Ta_2O_5 is a high-k oxide that has been studied as an etch mask for silicon,[1] as a dielectric layer in dynamic and resistive random access memories,[2,3] metal-oxide–semiconductor field effect transistors,[4] and many other applications. Hafnium-based dielectric materials are used on an industrial scale as gate dielectrics in complementary metal-oxide semiconductor transistors, and ZrO_2 and TiO_2 have also been considered as alternative high-k materials.[5] ZrO_2 is specifically used as a dielectric in dynamic random access memory.[6] As these materials are increasingly used in 3D structures such as gate-all-around transistors and 3D memory stacks, processes used to deposit and etch these materials need to operate isotropically, without a line of sight to the surface. In addition, etching needs to be selective to a given material.

Although plasma etching is well-known for the anisotropic reactive ion etching (RIE), it can also be used for isotropic etching.[7] Operation in remote plasma mode can provide fully isotropic etching as only a flux of neutral radicals is reaching the substrate. This also decreases plasma-induced damage to the substrate as it does not come into a direct contact with the plasma. However, plasma methods require careful control to maintain selectivity and can suffer from poor conformality due to recombination of the radical species. Chemical vapor etching (CVE) is a gentler approach, where gas phase etchants react with the substrate to form volatile compounds. The thermally activated reactions offer more selectivity through chemistry, and the etchant gas is inherently more stable than the transient radical species from plasma.

CVE methods have been developed for etching Si and SiO_2, as well as other oxides. These most often rely on using volatile fluorine compounds such as XeF_2 and HF to produce volatile fluorides as etch products.[8–10] These continuous etching methods can be modified to a cyclic etching process known as gas-phase pulsed etching (GPPE).[11,12] Here the etchant gas or vapor pulses are separated by inert gas purging periods, during which volatile etch products can be removed more efficiently. In GPPE the etch depth can be simply controlled by the number of etch cycles. The etch per cycle (EPC) is controlled by varying process parameters such as reactor temperature, etchant pulse and purge times, and partial pressure of the etchant.

Ta_2O_5 has previously been etched using $TaCl_5$ and an unspecified oxygen containing precursor, according to a patent by Dautartas and Sneh.[13] Etching of Ta_2O_5 by $TaCl_5$ has also been observed during atomic layer deposition (ALD) of Ta_2O_5 with $TaCl_5$ and H_2O.[14] When a corresponding Nb_2O_5 ALD process with $NbCl_5$ and H_2O was attempted it was seen that Nb_2O_5 was etched even more aggressively with $NbCl_5$.[15] Mechanistic studies[16] verified that the etching occurred according to the reaction:

$$3\ NbCl_5\ (g) + Nb_2O_5\ (s) \rightarrow 5\ NbOCl_3\ (g) \qquad (1)$$

Because of the chemical similarity of tantalum and niobium it is presumed that $NbCl_5$ etches Ta_2O_5 as well. Compared to

Department of Chemistry, University of Helsinki, FI-00014 Helsinki, Finland. E-mail: juha.t.ojala@helsinki.fi, mikko.ritala@helsinki.fi

$TaCl_5$, $NbCl_5$ has the advantage of being more abundant and affordable, although both tantalum and niobium are considered critical elements.

Several dry etching processes using plasma have been demonstrated for the group 4 oxides TiO_2, ZrO_2 and HfO_2,[17–19] but their selectivity is limited. Chemical vapor etching of TiO_2 has been demonstrated using HF and WF_6.[20,21] In the latter case, diffusion of fluorine into the subsurface TiO_2 layers was noticed. ZrO_2 and HfO_2 have been previously etched using atomic layer etching,[22,23] but few continuous CVE methods for these oxides have been published.

This study introduces $NbCl_5$ as a new etchant for GPPE of Ta_2O_5, TiO_2, and ZrO_2, with excellent selectivity to SiO_2, Al_2O_3, TiN, and HfO_2.

2. Experimental

Ta_2O_5, Al_2O_3, TiO_2, ZrO_2, and HfO_2 films used in the etching experiments were grown by atomic layer deposition on Si(100) in an F-120 ALD reactor (ASM Microchemistry Oy). Deionized water delivered from an external source was used as the oxygen precursor for the oxide film deposition. The metal precursors and deposition parameters are presented in Table 1. The metal precursors evaporated at room temperature were delivered from external sources with vacuum draw and the others were sublimed from glass boats inside the reactor. SiO_2 films were grown by oxidizing silicon wafers in air at 950 °C for 80 minutes. TiN films were received from a collaborating company. Measured film properties are shown in Table 2.

Etching experiments were conducted in the F-120 reactor with $NbCl_5$ (>99%, Strem Chemicals, Inc.) sublimed from a glass boat at 80 °C. The etchant was delivered to the sample in pulses followed by purge periods during which only N_2 was flowing over the substrate. Ta_2O_5 films deposited on 5 × 5 cm^2 silicon substrates were used for the etching experiments and 1 × 5 cm^2 coupons cleaved from larger pieces were used for studying the selectivity. As the sample cassette can house two 5 × 5 cm^2 substrates, native oxide covered silicon was used as the other substrate.

Film crystallinity was evaluated using a PANalytical X'Pert Pro MPD X-ray diffractometer with Cu Kα (λ = 1.54 Å) radiation and grazing incidence geometry. The same instrument was used for X-ray reflectivity (XRR) measurements.

Thicknesses of the films before and after etching were studied using ellipsometry (Filmsense FS-1 multi-wavelength ellipsometer with 465, 525, 590 and 635 nm wavelengths) and verified with XRR when possible. Ellipsometry measurements were taken from nine points on the sample in a 3 × 3 grid pattern. The etched thicknesses were calculated as a difference of film thicknesses before and after etching.

Table 2 Physical and chemical properties of the films used in the etching experiments. Refractive indices were measured with ellipsometry at 630 nm and densities using X-ray reflectivity. Impurity contents were measured using ToF-ERDA

Material	Crystal phase	Refractive index	Density (g cm^{-3})	Impurity contents (at-%)					
				C	N	H	Cl	O	Hf
Ta_2O_5	Amorphous	2.21	8.04	0.1	—	0.2	—	—	—
Al_2O_3	Amorphous	1.64	3.00	0.2	—	1.4	—	—	—
TiO_2 (300 °C)	Anatase	2.51	3.77	0.1	—	0.1	—	—	—
TiO_2 (150 °C)	Amorphous	2.40	3.85	0.1	—	0.2	0.5	—	—
ZrO_2	Cubic	2.11	5.63	0.9	0.4	1.5	—	—	0.5
HfO_2	Monoclinic	2.09	9.66	0.3	0.2	1.1	—	—	—
TiN	Cubic	—	5.09	—	—	0.8	0.6	9.2	—

Atomic force microscopy (AFM, Veeco Multimode V instrument) was used to study roughnesses of the films. A Si probe with a nominal tip radius of 10 nm and a spring constant of 40 N m^{-1} was used to capture images in air. Roughness was calculated as a root-mean-square value (R_q) from the flattened images. Flattening was performed to remove artefacts from the sample tilt and scanner bow.

Energy dispersive X-ray spectrometer (EDS, Oxford INCA 350) connected to a Hitachi S-4800 field-emission scanning electron microscope (FE-SEM) was used to study compositions of the etched films. Film compositions before etching were measured using ToF-ERDA with a 35 MeV ^{127}I-beam.

Elemental composition of the surface before and after etching was measured with X-ray photoelectron spectroscopy (XPS, PREVAC) with a monochromated Al Kα anode with a photon energy $h\nu$ = 1486.7 eV as an X-ray source, a hemispherical electron analyzer and a 2D spatial detector. For survey spectra 2.5 × 25 mm slit was used and for detail scan measurements a 0.8 × 25 mm slit with electron pass energy of 100 eV. The latter allows to acquire the FWHM 0.61 eV for the Ag 3d as a reference. During the measurements the vacuum level was 3 × 10^{-10} mbar. Some experiments were done *in vacuo* in a vacuum cluster with an ALD reactor directly connected to the XPS. Detailed description of the system has been published elsewhere.[24]

Etching mechanism was studied using a modified F-120 reactor equipped with a Maxtek TM-400 quartz crystal microbalance (QCM) and Hiden HAL/3F 501 RC quadrupole mass

Table 1 Metal precursors and process parameters used for depositing the metal oxide films for the etching experiments

Film	Metal precursor	Precursor temperature (°C)	Deposition temperature (°C)
Ta_2O_5	Tantalum ethoxide, $Ta(OEt)_5$	95	325
TiO_2	Titanium tetrachloride, $TiCl_4$	RT	150, 300
ZrO_2	Tetrakis(ethylmethylamido)zirconium, $Zr(NEtMe)_4$ (TEMAZr)	90	250
HfO_2	Tetrakis(ethylmethylamido)hafnium, $Hf(NEtMe)_4$ (TEMAHf)	40	250
Al_2O_3	Trimethylaluminum, $AlMe_3$ (TMA)	RT	200

spectrometer (QMS).[25] Mass spectra of $NbCl_5$ and etch products of Ta_2O_5 were measured by scanning the mass range of interest multiple times. During one scan the $NbCl_5$ etchant was supplied. The scans without the $NbCl_5$ supply were averaged and taken as a background that was subtracted from the mass spectrum measured during the $NbCl_5$ supply.

Thermodynamic calculations were carried out using HSC chemistry 7.11 software (Outotec). Equilibrium concentrations were calculated at 10 mbar pressure with the following starting materials: 5 kmol N_2 (g), 0.1 kmol $NbCl_5$ (g), and 0.01 kmol Ta_2O_5.

An FEI Quanta 3D 200i FIB-SEM was used to prepare test specimens for selective etching. A 30 kV/100 pA gallium ion beam was used with 38° ion-to-surface incident angle, thus lowering the extent and depth of gallium implantation and increasing milling rate. The same FIB-SEM system was used for preparing cross-section specimens with normal lift-out procedures. The Hitachi S-4800 FE-SEM was used for imaging the patterned structures and the lift-out specimens. As the patterned oxide film stacks are insulating, sputtered Au/Pd films were used to assist both SEM imaging and FIB lift-out sample preparation.

3. Results

3.1. Thermodynamic calculations

Thermodynamics of etching Ta_2O_5 with $NbCl_5$ were studied by calculating equilibrium concentrations at the temperature range of 0–400 °C (Fig. 1). Even though the real system is not in equilibrium during the etching, the equilibrium concentrations give an indication of the reaction products. Excess $NbCl_5$ was used compared to Ta_2O_5 to approximate the etching conditions. The amount of the etchant compared to N_2 and the total pressure of the system (10 mbar as in the experiments) corresponds approximately to the vapor pressure of $NbCl_5$, 0.8 mbar.

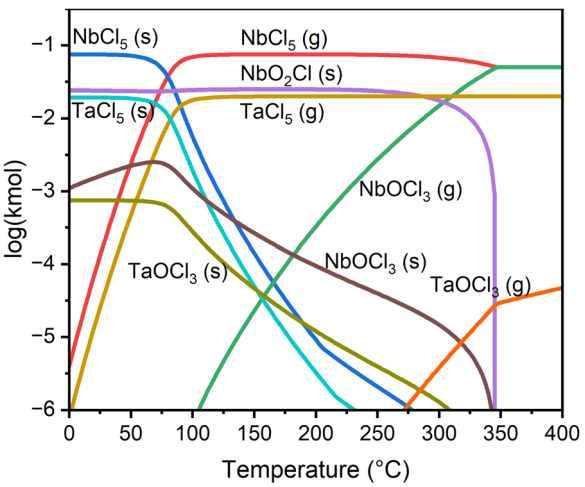

Fig. 1 Equilibrium amounts of different chemical species in the reaction of 0.1 kmol $NbCl_5$ and 0.01 kmol Ta_2O_5 calculated with HSC chemistry 7.11.

According to the calculations no Ta_2O_5 remains in the system under the equilibrium and even the solid TaO_2Cl is a very minor component (outside the graph range). At the low temperatures tantalum exists mostly as solid $TaOCl_3$ and $TaCl_5$, but above about 100 °C it is seen mainly as gaseous $TaCl_5$. Gaseous $TaOCl_3$ is also seen in low concentrations above 300 °C. Because there is an excess of $NbCl_5$ in the input, it is also the dominant Nb species for most of the temperature range. The most abundant reaction product below 300 °C is solid NbO_2Cl, with a minor component of solid $NbOCl_3$. Above 300 °C gaseous $NbOCl_3$ becomes the most abundant reaction product. This corresponds well to the observed etching onset temperature of 275 °C. The complete absence of Ta_2O_5 shows that it should always react with $NbCl_5$. The dominant species indicate that tantalum preferentially binds with chlorine, forming $TaCl_5$, and oxygen is removed as $NbOCl_3$ according to the reaction:

$$Ta_2O_5\ (s) + 5\ NbCl_5\ (g) \rightarrow 2\ TaCl_5\ (g) + 5\ NbOCl_3\ (g) \quad (2)$$

The Gibbs free energy changes for the reaction of $NbCl_5$ (g) and Ta_2O_5 to produce either $TaCl_5$ (g) or $TaOCl_3$ (g), along with etching reactions for Al_2O_3, SiO_2, TiO_2, ZrO_2, and HfO_2 are presented in Fig. 2. Reaction R2 that produces $TaCl_5$ is indeed thermodynamically much more favorable than reaction R3 that produces $TaOCl_3$. For the reaction R2, the Gibbs free energy change becomes negative above about 325 °C. It is also seen that etching of ZrO_2 and HfO_2 become favorable at similar temperatures, and etching of TiO_2 already at about 125 °C.

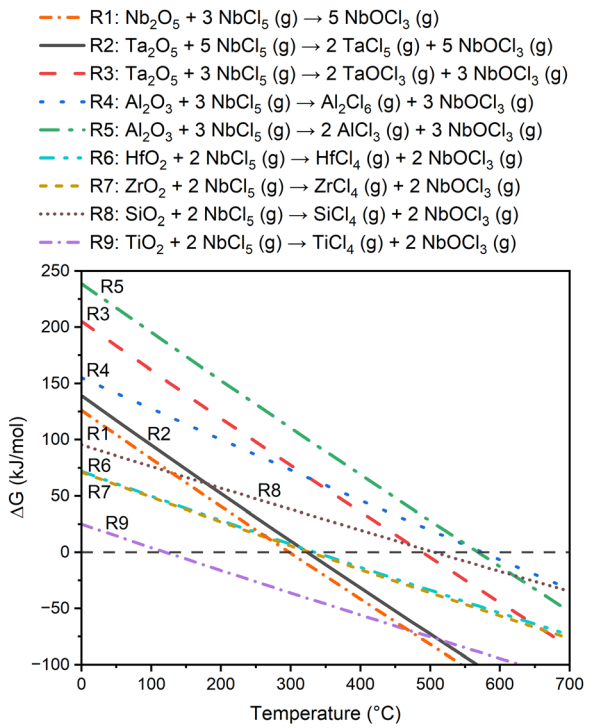

Fig. 2 Gibbs free energy changes for etching reactions of Nb_2O_5, Ta_2O_5, Al_2O_3, HfO_2, ZrO_2, SiO_2, and TiO_2 at the temperature range of 0–700 °C.

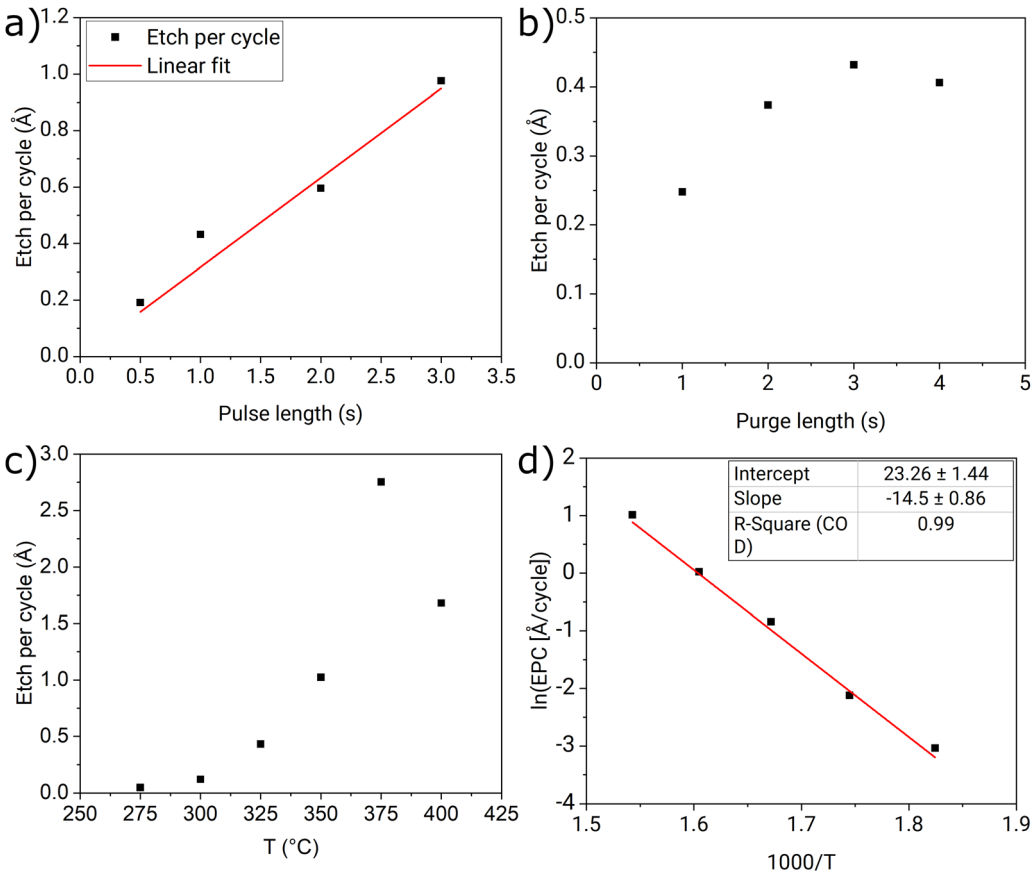

Fig. 3 Dependence of EPC at 325 °C on (a) pulse length when the purge length was 3 s, and (b) purge length with 1 s pulses. (c) EPC as a function of the etching temperature, and (d) Arrhenius plot of EPC. Etching cycles consisted of 1 s etchant pulse followed by 3 s purge period and the number of cycles was varied from 100 to 1000 depending on the temperature.

On the other hand, etching of SiO_2 and Al_2O_3 do not become favorable below 500 °C.

Equilibrium concentrations were also calculated for the etching of ZrO_2 and HfO_2. They formed very similar compounds at high temperatures, with MCl_4 (g) as the dominant species above 150 °C (M = Zr or Hf). Below this temperature there were slight differences: zirconium formed mostly solid $ZrCl_4$, whereas hafnium was seen as solid $HfOCl_2$ below 50 °C and solid $HfCl_4$ at 50–150 °C. These temperatures are far from the observed etching temperatures, but the results indicate some difference between zirconium and hafnium, which are generally very similar in their chemistry.

3.2. Etching of Ta_2O_5

Effects of the pulsing parameters on the etch per cycle (EPC) were studied at 325 °C and the results from the center of the substate are presented in Fig. 3. The length of the etchant pulse had a linear effect on EPC, which indicates constant etch rate per time unit: 0.32 Å s^{-1}. Etching with a continuous flow of $NbCl_5$ without pulsing gave a similar etch rate of 0.30 Å s^{-1}. The length of the purging period also had a significant effect on the EPC: increasing the purge length to 3 s increased the EPC from 0.25 Å to 0.42 Å (Fig. 3b). Sharma *et al.* saw a similar trend in GPPE of TiN with $SOCl_2$ and attributed the increase of EPC with the increasing purge length to a better recovery of the etchant pressure in the source and better removal of less volatile etch products during the extended purge.[11] The constant level reached in EPC with longer purge lengths can be attributed to the saturation of the etchant vapor in the source. The thermodynamic calculations indicate that etching of Ta_2O_5 proceeds *via* volatile $TaCl_5$ so the extended purge might drive the etching by removing the volatile products from the reactor. A cycle of 1 s $NbCl_5$ pulse and 3 s purge was chosen for the rest of the experiments.

The effect of the etching temperature was studied next. Fig. 3c shows the EPC at the temperature range of 275–400 °C. Fig. 3d shows an Arrhenius plot of the same results, that is a natural logarithm of EPC plotted against the inverse of the etching temperature. It can be seen that the process follows the Arrhenius type dependence at the temperature range of 275–375 °C, and an activation energy of 120 kJ mol^{-1} was estimated from the slope of a linear fit. Above 375 °C, the EPC begins to diminish: 1.68 Å per cycle at 400 °C *vs.* 2.75 Å per cycle at 375 °C. The reason could be that at high temperatures $NbCl_5$ is lost to side reactions or does not adsorb on the surface long enough for the reaction to take place.

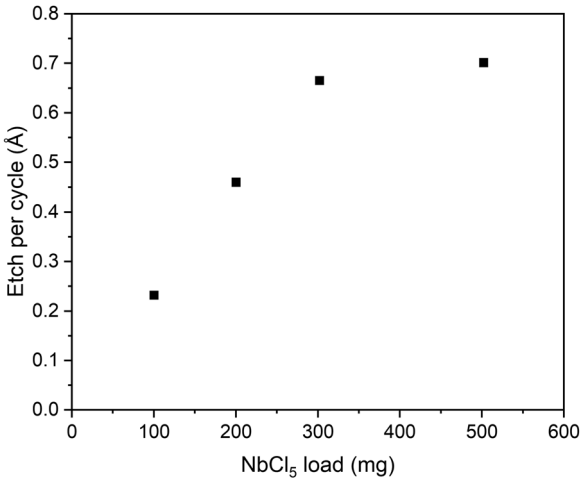

Fig. 4 Effect of $NbCl_5$ loading on EPC at 325 °C using 500 cycles of 1 s etchant pulses followed by 3 s purges.

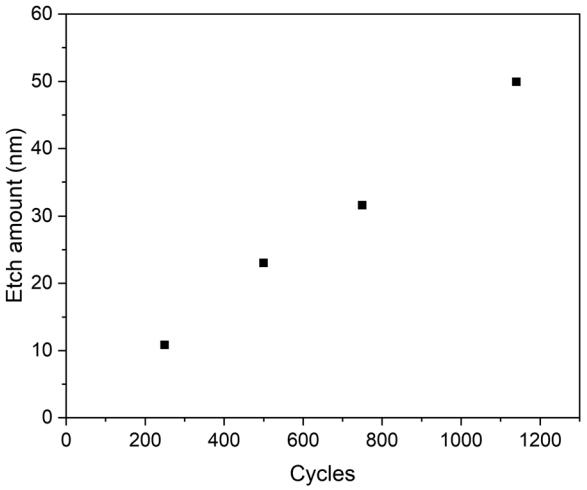

Fig. 5 Etch thickness as a function of the number of etch cycles at 325 °C. Cycles of 1 s $NbCl_5$ pulse and 3 s purge with 200 mg $NbCl_5$ loading.

The effect of the etchant load in the source boat was also studied (Fig. 4), and it was found that the EPC increases linearly with the mass of $NbCl_5$ loaded for the experiment until around 300 mg. The etchant did not run out in any of the experiments, so the increase of EPC is likely due to a faster regeneration of the etchant vapor in the source. Most of the experiments up to this point had been done using a 200 mg etchant load and this was kept constant to ensure that the results are comparable.

The reactor used in this study is of the cross-flow type. There was some profile in the etched thickness along the gas flow direction. The EPC was 2–14% higher at the etchant inlet side 1 cm from the substrate edge, and 6–17% lower at the exhaust side as compared to the center of the substrate. As the EPC follows Arrhenius dependence, the etch rate is reaction controlled and the profile is probably a result of the etchant being used up along the flow across the substrate. The etchant load did not have a significant effect on the profile, however. In shower-head and other top-flow reactors better uniformity is expected than in the cross-flow reactor used in this study.

Linearity of the etching was also studied with a series of 250–1140 etch cycles (Fig. 5). It is seen that the etch thickness follows the number of cycles linearly.

3.3. Film characterization

The films were amorphous according to XRD and no peaks were detected after partial etching either. After partial etching of the Ta_2O_5 films, elemental analysis with EDS detected only Ta, O, and C in the films, the last one being likely from atmospheric contamination. No Nb or Cl was detected with EDS. Measurements of the films with XPS after transferring the sample *in vacuo* from the reactor also showed Ta, O and C before etching, and a slight Cl residue after an etchant pulse. No Nb was detected in any of the samples. After complete etching of a Ta_2O_5 film at 325 °C, no Nb or Ta could be detected on the substrate with EDS. XPS did not show obvious peaks other than Si and O but a very small bump could be seen in the Ta 4f peak region, indicating trace amounts of tantalum left on the surface.

Roughnesses of the partially etched films were studied with AFM (Fig. 6), which showed a slight increase from around 0.2 nm R_q for the unetched film to 1.4 nm when 30 nm of the film was etched. Beyond that the roughness of the films remained constant. The roughness might be caused by surface restructuring during the etching or by inherent stochastic effects of continuous etching. Another possibility is that the

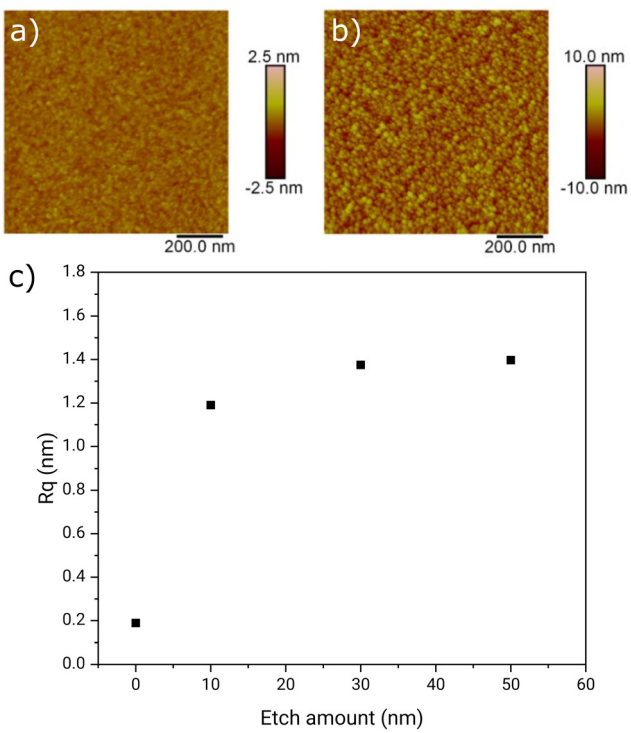

Fig. 6 AFM images of (a) an unetched 44 nm thick Ta_2O_5 film and (b) a film after etching away 30 nm of Ta_2O_5. (c) Roughnesses of the films etched to various depths at 325 °C as measured by AFM.

films had some small slower-etching crystalline domains which were too small to be detected with XRD.

3.4. Mechanistic studies

To study the etching mechanism, Ta_2O_5 was deposited and etched *in situ* using a modified F-120 reactor equipped with QMS and QCM, which has been described in detail elsewhere.[25] The mass spectrum of $NbCl_5$ was measured prior to Ta_2O_5 deposition and the observed peaks are presented in Table 3 along with the fragments they are attributed to. The signals of HCl and $NbOCl_3$ fragments are attributed to reactions with residual water in the reactor. The relative intensities of the species with the same number of Cl atoms corresponded to the natural abundances of ^{35}Cl and ^{37}Cl.

Mass spectrum measured during the etching showed quite weak signals but the most significant etch products were identified as $[TaCl_4]^+$ species, a fragment of $TaCl_5$, whereas $TaOCl_3$ and its fragments did not significantly exceed the background. Different *m*/*z* values corresponding to the etchant and etch products were monitored as a function of time during the etchant pulsing (Fig. 7). The masses 235 and 216, corresponding to $[NbCl_4]^+$ and $[NbOCl_3]^+$ respectively, show clear signals during the etchant pulses, as does *m*/*z* 323, which corresponds to $[TaCl_4]^+$. On the other hand, *m*/*z* 302 $[TaOCl_3]^+$ does not deviate from the background. This observation supports that $TaCl_5$, rather than $TaOCl_3$, is the primary etch product. It can also be seen that the first few etchant pulses register weaker in the QMS. This is probably due to the first pulse being mostly consumed in reactions with the hydroxyl terminated surfaces left after the deposition of Ta_2O_5.

Table 3 The most prominent *m*/*z* values detected in the mass spectrum of $NbCl_5$ and the fragments assigned to them

m/*z*	Fragment
36	$[H^{35}Cl]^+$
38	$[H^{37}Cl]^+$
178/179	$[NbO^{35}Cl_2]^+$
181	$[NbO^{35}Cl^{37}Cl]^+$
214	$[NbO^{35}Cl_3]^+$
216	$[NbO^{35}Cl_2{}^{37}Cl]^+$
218	$[NbO^{35}Cl^{37}Cl_2]^+$
233	$[Nb^{35}Cl_4]^+$
235	$[Nb^{35}Cl_3{}^{37}Cl]^+$
237	$[Nb^{35}Cl_2{}^{37}Cl_2]^+$

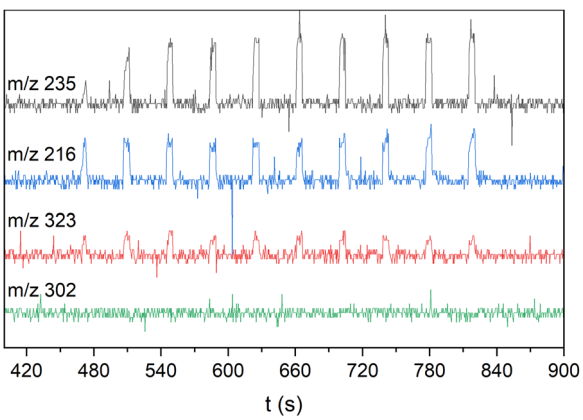

Fig. 7 QMS of $NbCl_5$ fragments and etch products of Ta_2O_5 during etching at 325 °C.

3.5. Etch selectivity

The selectivity of $NbCl_5$ as an etchant was studied with thermal SiO_2 and ALD grown Al_2O_3, TiO_2, ZrO_2, HfO_2 and TiN films. Both crystalline and amorphous TiO_2 films were studied. The Al_2O_3 films were amorphous and the ZrO_2, HfO_2, and TiN films were crystalline according to the XRD measurements. Etch rates at different temperature are presented in Fig. 8.

It was observed that SiO_2, Al_2O_3, and TiN were not etched to any significant degree. Some blistering of Al_2O_3 was observed at 350 and 400 °C (Fig. 9). Blistering of ALD Al_2O_3 films on silicon upon annealing has been observed previously in the literature. It is generally attributed to accumulation of hydrogen gas and/or water vapor at the interface as thick Al_2O_3 films act as diffusion barriers.[26–28] The origin of water in our Al_2O_3 films is dehydroxylation of hydroxyl impurities.[29] The EPC of ZrO_2

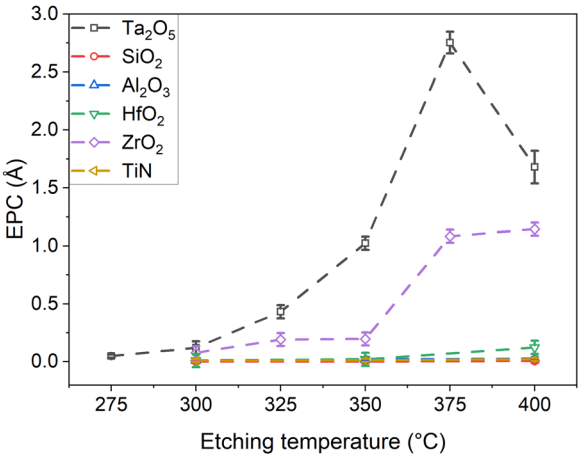

Fig. 8 EPC of selected materials with $NbCl_5$ at different etching temperatures using 1 s pulses and 3 s purges. Error bars were calculated based on an estimated error of 1 nm for each thickness measurement due to inherent measurement error and variation in the measurement location and minor film thickness variation.

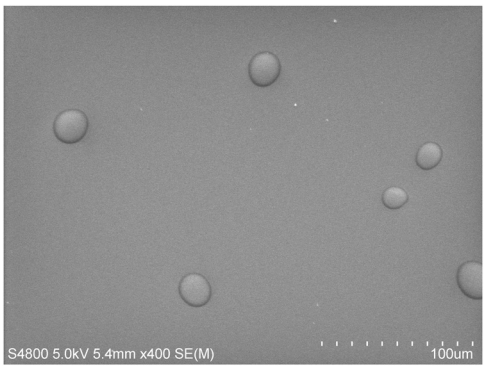

Fig. 9 SEM image of Al_2O_3 film after exposure to $NbCl_5$ at 350 °C.

was very low at 300 °C, but increased with the etching temperature and reached 1.1 Å at 400 °C. The EPC of HfO_2, on the other hand, was negligible throughout the temperature range of 300–400 °C. No niobium residue was detected with EDS in any of the films after partial etching, and no zirconium or niobium were detected on the substrate after complete etching of a ZrO_2 film at 400 °C.

The selectivity between ZrO_2 and HfO_2 is unexpected as these materials share many similar properties, and the thermodynamics of their etching reactions are almost identical (Fig. 2). On the other hand, previous studies on ALE of ZrO_2 and HfO_2 have also found significantly different etch rates for these materials.[22,30] Crystalline HfO_2 films especially are generally harder to etch than crystalline ZrO_2 films. These ALE processes were based on fluorination of the oxides followed by a ligand exchange with a chlorine containing compound. Lii-Rosales *et al.* studied the ligand exchange and onset temperatures of spontaneous etching of ZrF_4 and HfF_4 with $SiCl_2(CH_3)_2$, $SiCl(CH_3)_2H$, and $SiCl_4$. They found that the temperatures were consistently higher for HfF_4, but this was not commented on in any way.[31] Mullins *et al.* conducted density-functional theory studies on the fluorination of ZrO_2 and HfO_2 surfaces with HF, looking also for the temperature at which spontaneous etching of the oxide becomes preferable to the self-limiting reaction.[32] They found that the minimum energy for the spontaneous etching diminished with increasing temperature and this effect was faster for ZrO_2 than for HfO_2, resulting in a lower etching temperature for ZrO_2.

A patent by Horace Chandler[33] describes removal of $HfCl_4$ from $ZrCl_4$ by passing a mixture of these metal chloride vapors through a mixture of HfO_2 and ZrO_2 powders, upon which $HfCl_4$ preferentially reacts with ZrO_2 to form HfO_2 and $ZrCl_4$. In our thermodynamic equilibrium calculations, HfO_2 reacting with $NbCl_5$ formed a significant fraction of $HfOCl_2$ at low temperatures. ZrO_2, on the other hand, formed mostly $ZrCl_4$ with negligible amounts of $ZrOCl_2$. These observations imply that hafnium has a stronger preference for binding to oxygen over chlorine as compared with zirconium.

Complete etching of both amorphous and crystalline TiO_2 was possible, but it was found that the etching was very nonuniform and showed a counterintuitive profile where the film was etched slower at the side of the etchant inlet. Additionally, the films were significantly roughened or otherwise modified upon etching, and the same ellipsometry model could not be used to model the films before and after etching. Thus, determination of EPC was unreliable, but it could be seen to reach approximately 4 Å at 325 °C for crystalline TiO_2 (Fig. 10). The films were investigated with EDS, but no niobium or other residues could be detected. No titanium or niobium could be detected on the substrate after complete etching.

3.6. Pattern etching

The applicability of selective etching was studied using a 40 nm Ta_2O_5 film, on top of which was deposited 50 nm of Al_2O_3. A Ga^+ focused ion beam was used to locally remove Al_2O_3 from 2 μm wide areas to expose the underlying Ta_2O_5 for etching. The

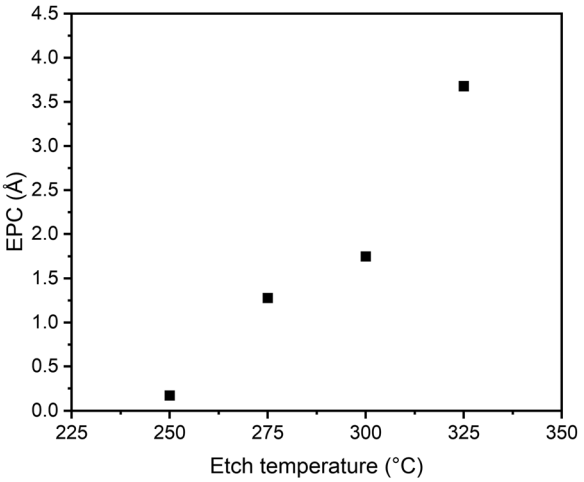

Fig. 10 Approximate EPC of crystalline TiO_2 films in the center of the substrate when etched with (1/3) s cycles of $NbCl_5$ at different temperatures.

amorphous films had sufficient thicknesses to fully protect the underlying silicon substrate from the gallium ions.

The patterned structure was etched with 2500 cycles of 1 s $NbCl_5$ pulse and 3 s purge at 325 °C. SEM images of the patterned film before and after the etching are presented in Fig. 11. Ta_2O_5 is seen brighter in the images due to the mass contrast of backscattered electrons. In the etched samples the brighter areas have receded from the pattern mask edges, and

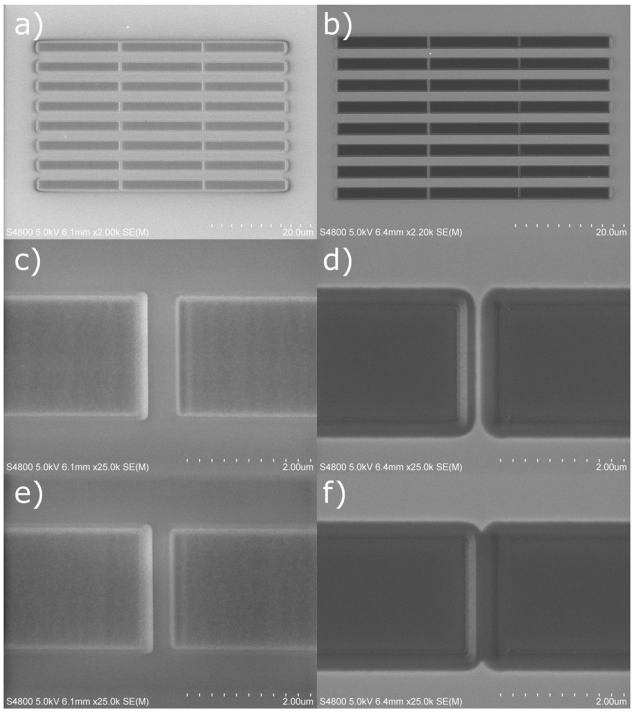

Fig. 11 SEM images of the pattern made with FIB on a Al_2O_3/Ta_2O_5 double layer (a) before and (b) after etching with 2500 cycles of $NbCl_5$. (c)–(f) show closeups of the overhang structures before (c) and (e) and after (d) and (f) the etching.

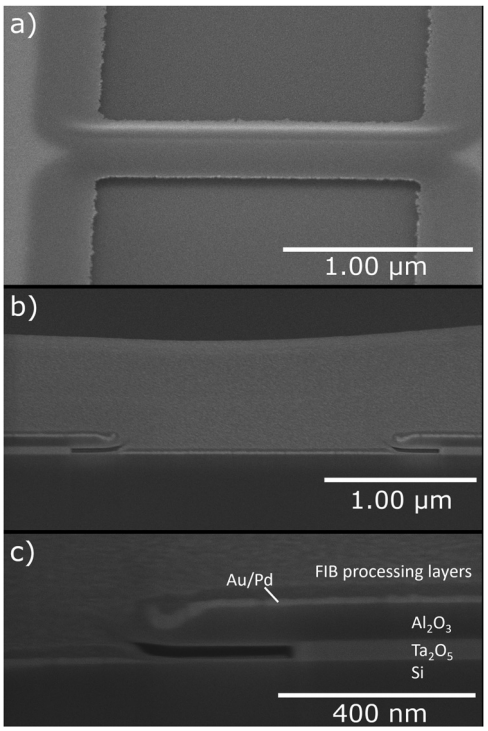

Fig. 12 (a) Overhang structure of a pattern after etching with $NbCl_5$ imaged with an electron beam at 60° angle to sample normal. (b) Lift-out sample cross-section of the etched sample along a line parallel to the scale bar in (a). (c) Close-up of the overhang structure at the Al_2O_3 mask edge with the different layers of the cross-section sample marked. Au/Pd was deposited to aid in imaging and sample preparation. The FIB processing layers denote Pt–C and (Pt,Ga)–C deposited in the FIB-SEM during the lift-out sample preparation. Some Pt–C is also seen deposited inside the overhang structure due to the lift-out process.

only weak contrast to the exposed substrate can be seen where the overhanging Al_2O_3 mask remains. Fig. 12 shows a tilted closeup of the etched sample and images of FIB-cut cross sections from the etched area of the sample.

The Al_2O_3 etch mask pattern had two narrow strips of different widths. Fig. 11(f) shows complete undercutting of the narrower strip whereas Fig. 11(d) shows that the etching stopped just before reaching complete removal of Ta_2O_5 underneath the wider Al_2O_3 strip. As seen from the undercut in the cross-section image in Fig. 12(c) and from the contrast in the top-view images of the etched sample in Fig. 11, the etch proceeded laterally about 270 nm. Based on the EPC of planar films, about 100 nm of lateral etch would be expected. The discrepancy can be explained by more etchant being available because only a small area was etched. It is also possible that some defects were left from the ion milling that increased the etch rate.

4. Conclusions

$NbCl_5$ was employed in a novel GPPE process for etching Ta_2O_5, ZrO_2, and TiO_2, with selectivity towards SiO_2, TiN and HfO_2. Slight roughening of the Ta_2O_5 films during the etching was observed, and *in vacuo* XPS measurements found some Cl on the surface after partial etching, but no niobium was left as an impurity. No residues could be detected with EDS on any of the films after partial etching or on the substrates after complete etching of the films.

Etching at 275–375 °C was found to follow an Arrhenius dependence on temperature and activation energy of the etching reaction was estimated to be 120 kJ mol^{-1}. Through thermodynamic calculations and QMS studies the etching reaction of Ta_2O_5 was identified as:

$$Ta_2O_5\ (s) + NbCl_5\ (g) \rightarrow TaCl_5\ (g) + NbOCl_3\ (g)$$

Selectivity was surprisingly found between ZrO_2 and HfO_2, with ZrO_2 being etched at 325–400 °C and HfO_2 showing negligible etch rates below 400 °C. Similar selectivity has however been noticed before in ALE with fluorination and ligand exchange. Based on these and other studies, it seems that halogenation of ZrO_2 is more favorable at lower temperatures than that of HfO_2. This is also supported by thermodynamic calculations in the present article.

The etching of TiO_2 was found to be very sensitive to film quality and temperature, with an inverted profile along the etchant flow. No clear reason for the poor etch characteristics was found, but the process is usable for complete removal of TiO_2 layers.

The etching of oxide materials and negligible impurities left on surfaces open new possibilities for research. Particularly, $NbCl_5$ could be employed as an etchant in ALE of metals and metal nitrides in an oxidation/etch type chemistry. Relevant materials for such studies are, for example, Ta, TaN, and TiN, which have been used in integrated circuits as electrodes and diffusion barriers in metal interconnects.

Data availability

Data is available upon request from the authors.

Conflicts of interest

There are no conflicts to declare.

Acknowledgements

The work was done under the ALD center of Finland infrastructure.

References

1 A. K. Chu, Y. S. Huang and S. H. Tang, *J. Vac. Sci. Technol., B*, 1999, **17**, 455–459.
2 K.-W. Kwon, C.-S. Kang, S. O. Park, H.-K. Kang and S. T. Ahn, *IEEE Trans. Electron Devices*, 1996, **43**, 919–923.
3 M.-J. Lee, C. B. Lee, D. Lee, S. R. Lee, M. Chang, J. H. Hur, Y.-B. Kim, C.-J. Kim, D. H. Seo, S. Seo, U.-I. Chung, I.-K. Yoo and K. Kim, *Nat. Mater.*, 2011, **10**, 625–630.
4 B. C. Lai, J.-C. Yu and J. Y.-M. Lee, *IEEE Electron Device Lett.*, 2001, **22**, 221–223.

5 J. Kumar, S. Birla and G. Agarwal, *Mater. Today Proc.*, 2023, **79**, 297–302.
6 D. Panda and T.-Y. Tseng, *Thin Solid Films*, 2013, **531**, 1–20.
7 H. Abe, M. Yoneda and N. Fujiwara, *Jpn. J. Appl. Phys.*, 2008, **47**, 1435.
8 C. S. Lee, J. T. Baek, H. J. Yoo and S. I. Woo, *J. Electrochem. Soc.*, 1996, **143**, 1099–1103.
9 D. E. Ibbotson, J. A. Mucha, D. L. Flamm and J. M. Cook, *J. Appl. Phys.*, 1984, **56**, 2939–2942.
10 H. F. Winters and J. W. Coburn, *Appl. Phys. Lett.*, 1979, **34**, 70–73.
11 V. Sharma, T. Blomberg, S. Haukka, S. Cembella, M. E. Givens, M. Tuominen, R. Odedra, W. Graff and M. Ritala, *Appl. Surf. Sci.*, 2021, **540**, 148309.
12 V. Sharma, S. Kondati Natarajan, S. D. Elliott, T. Blomberg, S. Haukka, M. E. Givens, M. Tuominen and M. Ritala, *Adv. Mater. Interfaces*, 2021, **8**, 2101085.
13 M. F. Dautartas and O. Sneh, *US Pat.*, US6037268A, 2000.
14 J. Aarik, K. Kukli, A. Aidla and L. Pung, *Appl. Surf. Sci.*, 1996, **103**, 331–341.
15 K.-E. Elers, M. Ritala, M. Leskelä and E. Rauhala, *Appl. Surf. Sci.*, 1994, **82–83**, 468–474.
16 K. Knapas, A. Rahtu and M. Ritala, *Chem. Vap. Deposition*, 2009, **15**, 269–273.
17 S. Norasetthekul, P. Y. Park, K. H. Baik, K. P. Lee, J. H. Shin, B. S. Jeong, V. Shishodia, E. S. Lambers, D. P. Norton and S. J. Pearton, *Appl. Surf. Sci.*, 2001, **185**, 27–33.
18 J.-C. Woo, S.-G. Kim, J.-G. Koo, G.-H. Kim, D.-P. Kim, C.-H. Yu, J.-Y. Kang and C.-I. Kim, *Proc. 1st Int. Conf. Microelectron. Plasma Technol. ICMAP 2008*, 2009, **517**, 4246–4250.
19 T. Maeda, H. Ito, R. Mitsuhashi, A. Horiuchi, T. Kawahara, A. Muto, T. Sasaki, K. Torii and H. Kitajima, *Jpn. J. Appl. Phys.*, 2004, **43**, 1864.
20 S. K. Natarajan, A. M. Cano, J. L. Partridge, S. M. George and S. D. Elliott, *J. Phys. Chem. C*, 2021, **125**, 25589–25599.
21 P. C. Lemaire and G. N. Parsons, *Chem. Mater.*, 2017, **29**, 6653–6665.
22 J. A. Murdzek and S. M. George, *J. Vac. Sci. Technol., A*, 2020, **38**, 22608.
23 Y. Lee and S. M. George, *J. Phys. Chem. C*, 2019, **123**, 18455–18466.
24 H.-E. Nieminen, M. Chundak, M. J. Heikkilä, P. R. Kärkkäinen, M. Vehkamäki, M. Putkonen and M. Ritala, *J. Vac. Sci. Technol., A*, 2023, **41**, 022401.
25 A. Rahtu and M. Ritala, in *Proceedings of the Fifteenth International Symposium on Chemical Vapor Deposition*, ed. M. Allendorf and M. Hitchman, The Electrochemical Society, 2000, vol. 13, pp. 105–111.
26 B. Vermang, H. Goverde, A. Lorenz, A. Uruena, G. Vereecke, J. Meersschaut, E. Cornagliotti, A. Rothschild, J. John, J. Poortmans and R. Mertens, in 2011 37th IEEE Photovoltaic Specialists Conference, 2011, pp. 003562–003567.
27 S. Li, P. Repo, G. von Gastrow, Y. Bao and H. Savin, in 2013 IEEE 39th Photovoltaic Specialists Conference (PVSC), 2013, pp. 1265–1267.
28 L. Hennen, E. H. A. Granneman and W. M. M. Kessels, in 2012 38th IEEE Photovoltaic Specialists Conference, 2012, pp. 001049–001054.
29 C. Guerra-Nuñez, M. Döbeli, J. Michler and I. Utke, *Chem. Mater.*, 2017, **29**, 8690–8703.
30 Y. Lee, C. Huffman and S. M. George, *Chem. Mater.*, 2016, **28**, 7657–7665.
31 A. Lii-Rosales, V. L. Johnson, A. S. Cavanagh, A. Fischer, T. Lill, S. Sharma and S. M. George, *Chem. Mater.*, 2022, **34**, 8641–8653.
32 R. Mullins, S. Kondati Natarajan, S. D. Elliott and M. Nolan, *Chem. Mater.*, 2020, **32**, 3414–3426.
33 H. Chandler, *US Pat.*, US3276862A, 1966.